WILEY-VCH

DOI: 10.1002/((please add manuscript number))
Article type: Full Paper

Remarkably Enhanced Hydrogen Generation of Organolead Halide Perovskites via Piezocatalysis and Photocatalysis

*Mengye Wang,[1,2] Yunpeng Zuo,[2] Jingli Wang,[2] Yi Wang,[2] Xinpeng Shen,[2] Bocheng Qiu,[2] Lejuan Cai,[2] Feichi Zhou,[2] Shu Ping Lau[2] and Yang Chai[2,3]**

Prof. Dr. M. Wang
State Key Laboratory of Optoelectronic Materials and Technologies, School of Materials, Sun Yat-sen University, Guangzhou, 510275, People's Republic of China

Prof. Dr. M. Wang, Y. Zuo, Dr. J. Wang, Y. Wang, X. Shen, Dr. B. Qiu, L. Cai, Dr. F. Zhou, Prof. Dr. S. P. Lau and Prof. Dr. Y. Chai
Department of Applied Physics, The Hong Kong Polytechnic University, Hung Hom, Kowloon, Hong Kong, People's Republic of China
E-mail: ychai@polyu.edu.hk

Prof. Dr. Y. Chai
The Hong Kong Polytechnic University Shenzhen Research Institute, Shenzhen, People's Republic of China

Keywords: Piezophoto-catalysis, $CH_3NH_3PbI_3$ perovskite, piezoelectrics, hydrogen generation

Abstract

To alleviate photo-induced charge recombination in semiconducting nanomaterials represents an important endeavor towards high-efficiency photocatalysis. Here we report a judicious integration of piezoelectric and photocatalytic properties of organolead halide perovskite $CH_3NH_3PbI_3$ ($MAPbI_3$) to enable a piezophoto-catalytic activity under simultaneous ultrasonication and visible light illumination for markedly enhanced photocatalytic hydrogen generation of $MAPbI_3$. The conduction band minimum of $MAPbI_3$ is higher than hydrogen generation potential (0.046 V *vs* normal hydrogen electrode), thereby rendering efficient hydrogen evolution. In addition, the non-centrosymmetric crystal structure of $MAPbI_3$ enables its the piezoelectric property. Thus, $MAPbI_3$ readily responds to external mechanical force, creating a built-in electric field for collective piezophoto-catalysis as a result of effective separation of photo-generated charge carriers. Our experimental results show that $MAPbI_3$ powders exhibit superior piezophoto-catalytic hydrogen

generation rate (23.30 μmol h^{-1}) in HI solution upon concurrent light and mechanical stimulations, much higher than that of piezocatalytic (*i.e.*, 2.21 μmol h^{-1}) and photocatalytic (*i.e.*, 3.42 μmol h^{-1}) hydrogen evolution rate as well as their sum (*i.e.*, 5.63 μmol h^{-1}). The piezophoto-catalytic strategy provides a new way to control the recombination of photo-induced charge carriers by cooperatively capitalizing on piezocatalysis and photocatalysis of organolead halide perovskites to yield highly efficient piezophoto-catalysis.

1. Introduction

Photocatalytic hydrogen (H_2) evolution via utilizing semiconductor catalysts has been widely recognized as a highly viable route to clean and sustainable energy. [1] However, due to the rapid recombination of photo-generated charge carriers, photocatalytic H_2 generation is often plagued by the low quantum efficiency.[2] To this end, many efforts have been devoted to tackling this fundamental issue. One common strategy is to construct *p-n* junction photocatalysts, which render efficient separation of photo-induced electrons and holes and enhance photocatalytic performance.[3] Notably, a bias potential can also be imposed on photocatalytic electrodes to promote the separation of charge carriers.[4] Nonetheless, these approaches either require more than one semiconductor that potentially lead to complex catalyst preparation and high cost, or are solely applicable for the electrode catalysts instead of the powder counterparts.

It is notable that a built-in electric field in photocatalysts provides a driving force for efficient separation of photogenerated electrons and holes. [5] In a piezoelectric material, an internal electric filed can be generated due to the intrinsic piezoelectric effect.[6] Under a mechanical stretch or strain, piezoelectric materials display a built-in electric field resulting from the separation of positive and negative charge centers.[7] Driven by this field, upon illumination of piezoelectric materials, photo-generated electrons and holes move towards the opposite directions, leading to efficient charge separation and enhanced catalytic performance.[8] Due to their appealing optoelectronic properties

including tunable direct bandgaps, broadband absorption, high ambipolar mobility and defect tolerance, and the ease of solution processing, ABX_3 perovskites (A = methylammonium (MA^+), formamidinium (FA^+), Cs^+, or their combination, B^{2+} = Pb^{2+}, Sn^{2+}, etc., and X^- = Cl^-, Br^-, and I^-) have received much attention over the past decade.[9] They find applications in solar cells,[10] photovoltachromic supercapacitors,[11] photodetectors,[12] laser,[13] *etc*. Although $CH_3NH_3PbI_3$ ($MAPbI_3$) perovskites possess a noncentrosymmetric polarized structure and thus intriguing piezoelectric response,[14] their use for catalysis has not to be largely explored.

Here, we report a simple yet robust strategy to greatly enhance the photocatalytic H_2 evolution of organolead halide perovskite $CH_3NH_3PbI_3$ ($MAPbI_3$) by judiciously combining its piezoelectric and photocatalytic properties via concurrent application of mechanical force and light illumination (*i.e.*, a synergistic piezophoto-catalysis). $MAPbI_3$ manifests an appropriate band structure for hydrogen evolution and piezoelectric response, as evidenced by UV-vis, ultraviolet photoelectron spectroscopy and piezoelectric force microscopy measurements. We investigate the piezophoto-catalytic activities of $MAPbI_3$ at different ultrasonic powers. Particularly, at optimal ultrasonic power with light irradiation (*i.e.*, piezophoto-catalysis), $MAPbI_3$ demonstrates nearly 7-fold and 11-fold enhancement of H_2 generation over photocatalysis (*i.e.*, under light irradiation only) and piezocatalysis (*i.e.,* with ultrasonication at optimal power solely) of $MAPbI_3$, respectively. In conjunction with ultrasonication, hydrogen bond between MA^+ ion and Pb-I scaffold is weakened under light irradiation, leading to a more polarized structure of $MAPbI_3$ with aligned MA^+ ion. Consequently, a large electric field is generated, further preventing the recombination of charge carriers and thus promoting the catalytic activity of $MAPbI_3$.

2. Results and Discussion

2.1. Materials characterization

Figure S1 depicts the preparation procedure of $MAPbI_3$ powders via an anti-solvent approach. Prior to piezocatalytic, photocatalytic and piezophotocatalytic measurements, the $MAPbI_3$ powders

were placed in the $MAPbI_3$-saturated HI solution, and ultrasonicated for 1 h to ensure the retention of particle sizes during catalysis. The high-resolution TEM (HR-TEM) of $MAPbI_3$ shows the lattice fringes of 0.278 nm and 0.311 nm, corresponding to the (310) and (220) planes, respectively, of a tetragonal $MAPbI_3$ (**Figure 1a**). The XRD pattern of $MAPbI_3$ is displayed in **Figure 1b**, where the diffraction peaks can be indexed to tetragonal $MAPbI_3$, consistent with the HRTEM measurement.

UV-vis absorbance and ultraviolet photoelectron spectroscopy (UPS) studies were carried out to examine the band diagram of $MAPbI_3$. As-prepared $MAPbI_3$ absorbs nearly all visible light (**Figure 1c**), exhibiting a black color (**Figure S2a**). The optical bandgap of $MAPbI_3$ is 1.57 eV (**Figure S2b**), which agrees well with our simulation result (**Figure S2c**). On the basis of the UPS spectra (**Figure 1d)**, the work function (ϕ_m) of $MAPbI_3$ is extracted from the onset energy in the cut-off region, which is 4.27 eV ($\phi_m = h\upsilon$ -W= 21.2 eV -16.93 eV = 4.27 eV) with respect to the vacuum level (**Figure 1d)**. In the valence band region, the valence band maximum (VBM) at the binding energy of 1.47 eV is found, lower than the Fermi level (**Figure 1e)**. Thus, the VBM is determined to be -5.74 eV with respect to the vacuum level. Consequently, the conduction band minimum (CBM) is calculated to be -4.17 eV with respect to the vacuum level. The band diagram of as-prepared perovskite is sketched in the inset of **Figure 1e**. The VBM and CBM of $MAPbI_3$ are 1.24 V and -0.33 V versus the normal hydrogen electrode (NHE), respectively. As depicted in **Figure 1f**, the band structure of $MAPbI_3$ is well suitable for hydrogen evolution as the CBM of $MAPbI_3$ is higher than the hydrogen generation potential (*i.e.*, 0.046 V *vs* NHE). In addition, the VBM is lower than the oxidation potential (0.376 V *vs* NHE) of the reaction (*i.e.*, $3I^- + 2h^+ = I_3^-$), so I^- ions serve as sacrificial agents of photo-generated holes. During the catalytic process, holes oxidize I^- ions into I_3^- ions and electrons reduce H^+ ions into H_2.

The piezoelectric properties of $MAPbI_3$ were studied by piezoelectric force microscopy (**Figure 2**). The tip of piezoelectric force microscopy (PFM) scanned across a 0.7×0.7 μm^2 surface area to measure the piezo-response potential of $MAPbI_3$. **Figure 2a** shows a representative three-

dimensional view of $MAPbI_3$ film surface topography, displaying a quantitative height signal and the detailed surface of $MAPbI_3$ film. Concurrently, PFM amplitude is acquired from the same region (**Figure 2b**), revealing that piezoelectric response was created in $MAPbI_3$ under an externally compressive loading by PFM.

2.2. Piezophoto-catalytic hydrogen evolution

As the dark color of I_3^- adversely affects the light absorption of $MAPbI_3$, an electrochemical reduction was performed to eliminate the existing I_3^- ions in the solution prior to piezocatalytic, photocatalytic and piezophotocatalytic measurements. As the electrochemical reduction time increases, the solution color changes from black to light yellow (**Figure 3**). As the molar ratio of generated H_2 to I_3^- is unity according to the following reactions $3I^- + 2h^+ = I_3^-$ and $2H^+ + 2e^- = H_2$, the amount of evolved H_2 can be monitored through estimating the concentration change of I_3^-. The concentration of I_3^- can be calculated by substituting the absorbance at 353 nm into the I_3^- standard curve at 353 nm (**Figure S3**).[15] Prior to all the catalytic procedures, the quartz vessel is irradiated by ultrasonic wave under dark for 1 h in order to maintain the size uniformity of $MAPbI_3$ during the catalytic process, and reach dynamic equilibrium between precipitation and dissolution of $MAPbI_3$. With narrow band gap (**Figure 1c**), piezoelectric characteristics, and appropriate band structure to generate hydrogen (**Figure 1f**), perovskite $MAPbI_3$ can efficiently produce hydrogen under concurrency of visible light and ultrasonic stimulation. During the ultrasonic process, strains imposed on $MAPbI_3$ comprises two parts: one is introduced by the periodic acoustic pressure created from the ultrasonic wave, and the other is produced by the collapse of the acoustic cavitation walls of bubbles.[5a] During the ultrasonic process, extremely active bubbles are generated in water and then collapse, leading to high local pressure.[16] These two mechanical strains initiate the deformation of $MAPbI_3$. As a result, polarized electric dipoles are formed within $MAPbI_3$, leading to a built-in electric field.[5a, 16] Meanwhile, under light illumination, photo-generated electrons and holes are driven towards the opposite reaction sides to participate the redox reactions in response to the formed internal piezoelectric potential (*i.e.*, built-in electric field). Such

spatial separation drastically reduces the combination of photo-generated charge carriers, favoring the photocatalytic performance of $MAPbI_3$. In addition, the ultrasonication periodically alters the polarization direction, preventing piezoelectric polarized charges from being fully screened by the carriers from the electrolyte.

The piezophoto-catalytic performance of $MAPbI_3$ is exploited under constant visible light irradiation in conjunction with ultrasonication at different powers (*i.e.,* 50, 60, 70, 80, and 90 W) to catalytically produce H_2 (**Figures 4a** and **S4**). Clearly, the amount of hydrogen increases as a function of piezophoto-catalytic reaction time (**Figure 4a**), yielding the hydrogen evolution rate of $MAPbI_3$ is 6.50, 11.31, 23.30, 10.23, and 0.74 μmol h^{-1} at the ultrasonic power of 50, 60, 70, 80, and 90 W, respectively (**Table S1**). A remarkable increase of catalytic activity of $MAPbI_3$ is found when the ultrasonic power increased from 50 W to 70 W. This is not surprising as larger ultrasonic power resulted in greater deformation of $MAPbI_3$, thus a higher internal electric field is created, facilitating more effective separation of photo-excited electrons and holes.[5a] When the ultrasonic power was further raised from 70 W to 90 W, the hydrogen generation rate, however, decreased, which may be attributed to the higher excessive mechanical stress experienced under higher ultrasonic power. After piezophoto-catalysis for 2 h, the amount of hydrogen evolution reaches 12.70, 22.49, 46.07, 20.80, and 1.43 μmol by capitalizing on ultrasonic power of 50, 60, 70, 80, and 90 W, respectively (**Figure 4b**). It is worth noting that the hydrogen produced at 70 W is more than 32-fold that of at 90 W. Clearly, 70 W represents the optimal ultrasonic power for piezophoto-catalytic hydrogen evolution. This observation manifests a delicate trade-off between catalytic performance of $MAPbI_3$ and its stability in determining the proper ultrasonic power to generate mechanical stress. Gas chromatography (GC) was utilized to assess the amount of hydrogen evolved, which can be accurately obtained by measuring the I_3^- concentration (**Figure S5** and **Table S2**). The piezophoto-catalytic mechanism is schematically illustrated in **Figure 4c**. Under the application of mechanical force, dipole moments are created due to the lattice displacement and an

internal polarized electric field is thus formed. Driven by this polarization-induced potential, photo-generated electrons and holes move towards the opposite direction. As a consequence, the recombination of charge carriers is prevented and the photocatalytic activity of $MAPbI_3$ is largely improved.

In order to compare the piezo-, photo- and piezophoto-catalysis of $MAPbI_3$, the catalytic activity is evaluated under ultrasonic irradiation only, visible illumination solely, and concurrent ultrasonic and visible irradiation, respectively (**Figure 4d** and **S6**). The optimal ultrasonic power of 70 W was implemented. The hydrogen generation rate is 2.21, 3.42, and 23.30 μmol h^{-1} for piezo-, photo- and piezophoto-catalysis, respectively (**Table S3**). When the catalytic time proceeds to 2 h, the amounts of hydrogen produced by piezo-, photo- and piezophoto-catalysis are 4.57, 6.88, and 46.07 μmol, respectively (**Figure 4e**). It is clear that the hydrogen generation rate via piezophoto-catalysis is much higher than the sum of that via respective piezo- and photo- catalysis *(i.e.*, 11.45 μmol), signifying the synergy of concurrent light irradiation and ultrasonication in yielding robust piezophoto-catalysis. We note that light illumination weakens the hydrogen bond between the MA cation and the Pb-I scaffold, and reduces the rotation barrier of MA cation.[17] As a result, a more polarized structure of $MAPbI_3$ is formed, leading to the spontaneous electric potential of higher intensity and thus much higher catalytic activity.

The potential reusability of $MAPbI_3$ in $MAPbI_3$-saturated HI solution is estimated by three cycles of piezophototronic H_2 evolution for 5 h. During the three catalytic processes, the hydrogen generation rates keep nearly unchanged (**Figures 4f** and **S7a-S7c**). **Figure S7d** shows the XRD spectra of $MAPbI_3$ before and after each catalytic cycle. Negligible change is observed in the crystalline phase (**Figure S7d)**. **Figures S7e** and **S7f** show TEM and HR-TEM images of catalysts after three repeated catalytic cycles, respectively. The lattice fringes of 0.278 nm and 0.311 nm are in accordance with the interplanar spacing of the (310) and (220) planes of tetragonal $MAPbI_3$, respectively (**Figure S7f)**, which remains the same as those measured before catalysis (**Figure 1a**).

Figure S8 shows XRD patterns of $MAPbI_3$ after ultrasound and light excitation for different time when the ultrasonic power is 70 W. $MAPbI_3$ is measured once each hour in $MAPbI_3$-saturated HI solution. Peak positions of $MAPbI_3$ remain unchanged in piezophoto-catalysis for 10 h (**Figure S8**), indicating the high stability of $MAPbI_3$ in our catalytic system. The above observations indicate that $MAPbI_3$ remains its high activity in piezophoto-catalysis and exhibits a long-term stability in $MAPbI_3$-saturated HI aqueous solution.

2.3. Theoretical calculations

The possible underlying mechanism for the existence of the optimal ultrasonic power for piezophoto-catalysis is proposed below. Firstly, the increasing pressure (under the ultrasonic power from 50 W to 70 W) results in the larger electric field to separate the photo-induced electrons and holes, thus improving the catalytic efficiency. Secondly, and the original tetragonal phase of $MAPbI_3$ was found to convert into orthorhombic phase under excessive pressure (with ultrasonic power from 70 W to 80 W),[18] which is also confirmed by our density function theory (DFT) calculation (**Figures 5a, 5b** and **Table S4**). Unlike tetragonal $MAPbI_3$, orthorhombic $MAPbI_3$ does not possess the piezoelectric property, thereby displaying the decreased piezophoto-catalytic performance. **Figure 5c** shows that iodine (I) and lead (Pb) contribute to the density of states (DOS) of $MAPbI_3$ while the organic cation $CH_3NH_3^+$ has marginal contribution to the CBM and VBM. It is clear that the higher pressure triggers the band gap of $MAPbI_3$ to change from 1.51 eV (tetragonal phase) to 1.65 eV (orthorhombic phase), leading to the reduced utilization efficiency of light and thus further decreasing catalytic performance. Lastly, we note that the catalytic performance of $MAPbI_3$ rapidly declines when the ultrasonic power further increases to 90 W. This is due likely to the fact that further increasing ultrasonic power applied on $MAPbI_3$ may separate $MAPbI_3$ into crystalline and amorphous regions,[18] thereby greatly weakening and even diminishing its catalytic activity.

3. Conclusions

In summary, we developed a robust strategy via integrating piezoelectric effect and photocatalytic activity of perovskite $MAPbI_3$ to yield a synergistic piezophoto-catalysis for markedly enhanced hydrogen generation. $MAPbI_3$ possesses a favorable band structure for catalytic hydrogen generation and displays a piezoelectric property, as revealed by UPS and PFM measurements, respectively. In this study, ultrasonic vibration is implemented to exert periodic strain on $MAPbI_3$ and thus produce internal polarized electric field. Such internal electric field of $MAPbI_3$ imparts the effective separation of photo-induced charge carriers. There exists an optimal ultrasonic power, above which the piezophoto-catalytic activity of $MAPbI_3$ declines. According to the DFT calculations, the decreased catalytic performance is probably attributed to phase conversion of $MAPbI_3$ from piezo-active tetragonal into piezo-inactive orthorhombic as well as the low utilization efficiency of light. It is important to note that due to the strong polarization of $MAPbI_3$ at optimal ultrasonic power of 70 W, a highest piezophoto-catalytic hydrogen generation rate is resulted in, demonstrating nearly 7-fold and 11-fold improvement over that of sole photocatalysis and piezo-catalysis, respectively. Notably, under light irradiation the hydrogen bond between MA^+ ion and Pb-I scaffold could be weakened, rendering the formation of a more polarized structure with aligned MA^+ ion. Thus, a larger electric field is formed in $MAPbI_3$, preventing the recombination of charge carriers and further enhancing its catalytic activity. Clearly, combining piezo-catalysis and photo-catalysis of semiconductor photocatalysts possessing intrinsic piezoelectric property to attain a collective piezophoto-catalysis may represent an appealing strategy for efficient solar energy conversion, including water splitting, organic fuel production, among other areas.

4. Experimental Section

Preparation of $MAPbI_3$ powder: Methylammonium iodine (MAI) and PbI_2 of 1:1 molar ratio were dissolved in anhydrous *N,N*-dimethylformamide (DMF) to yield a yellow solution. $MAPbI_3$ powders were formed by adding chlorobenzene (CBZ) into the yellow solution at a 5:1 volume ratio.

The solvents were removed by centrifugation at 8000 rpm for 10 min, obtaining $MAPbI_3$ powders (**Figure S1**). The product was then collected and dried in a vacuum oven at 70 °C overnight.

Characterizations: Unless otherwise specified, $MAPbI_3$ noted in this section refers to $MAPbI_3$ after ultrasonication in the $MAPbI_3$-saturated HI solution for 1 h. The morphology of $MAPbI_3$ was assessed by transmission electron microscope (TEM, JEOL JEM-2100F). X-ray diffraction (XRD, Rigaku SmartLab) and scanning transmission electron microscope (STEM, JEOL JEM-2100F) were utilized to analyze the crystalline structure of $MAPbI_3$. The optical transmittance of $MAPbI_3$ was examined by UV-vis spectrophotometer (Shimadzu, UV-2550). The ultraviolet photoelectron spectroscopy (UPS) measurement was performed using He-I resonance lamp (21.2 eV) at room temperature. A bias potential of 5 V was applied on the sample when recording the secondary electron cutoff. The piezoelectricity of $MAPbI_3$ was characterized by atomic force microscopy (Bruker NanoScope 8) using piezoelectric force microscopy (PFM) mode.

The photocatalytic measurement of $MAPbI_3$ was tested in the HI aqueous solution. The aqueous HI solution was prepared as follows. A H-shaped cell was employed to separate the anode and cathode compartment with a Nafion 117 membrane placed between them (**Figure S2**). 15 mL of 57 wt% HI solution was added in each compartment. The carbon fiber paper with an active area of 2 cm^2 was utilized as both the working and counter electrodes. After Ar gas purging into two compartments for 15 min, -0.8 A of current was applied on the working electrode for 8 h. The color of HI electrolyte grew lighter with the increase of electrochemical reduction time (**Figure S2**). Then, 50 mg $MAPbI_3$ powders were added into 5.5 mL as-prepared HI solution. The photocatalytic hydrogen generation of $MAPbI_3$ was conducted in an ultrasonic generator (*i.e.*, 50 W, 60 W, 70 W, 80 W and 90 W) with or without visible light illumination. The reaction temperature was kept at 28 °C. The visible light was provided by a tungsten-halogen lamp (500 W with a light intensity of 100 mW cm^{-2}). At different irradiation time intervals, 25 μL HI solution was collected and diluted to 25 mL by deionized water. The hydrogen evolution amount was evaluated by monitoring the

concentration change of I_3^- in diluted HI solution via UV-vis spectrophotometer at the wavelength of 353 nm. The absorbance at 353 nm was compared to a standard curve of I_3^- solution to calculate the concentration of I_3^- in the solution. The standard curve of I_3^- was obtained by diluting the standard I_2 solution with 0.01 M KI solution to a required concentration. The amount of generated H_2 gas was also verified by gas chromatography (GC).

Simulation : The first principle calculations were conducted with Quantum ESPRESSO (QE). The generalized gradient approximation (GGA) Perdew-Burke-Ernzerhof (PBE) exch-corr was selected as the pseudopotential functional type. 2×2×2 tetragonal super cell (a = 9.10 Å, b = 9.02 Å, c = 13.1655 Å) of $MAPbI_3$ was used in the DFT calculation. The stress-dependent band structures were observed in the simulation. $MAPbI_3$ under 0 GPa and 2 GPa were calculated. $MAPbI_3$ under different stress along z-axis were calculated by changing the lattice parameters. The lattice parameter is determined by the stress and Young's modulus of $MAPbI_3$.[19] The stressed supercells were fully relaxed and optimized on the other two axes to the thermodynamically favored condition. The convergence threshold on total energy is 10^{-6} *a.u.* and the one on forces is 10^{-3} *a.u.*. The kinetic energy cutoff for wavefunctions is 50 Ry, and the kinetic energy cutoff for charge density and potential is 200 Ry.

Supporting Information

Supporting Information is available from the Wiley Online Library or from the author.

Acknowledgements

This work was supported by Science, Technology and Innovation Commission of Shenzhen (20180038) and the Hong Kong Polytechnic University (1-ZVGH and G-YBPS). M. W. gratefully acknowledges the support from Sun Yat-Sen University.

Received: ((will be filled in by the editorial staff))
Revised: ((will be filled in by the editorial staff))
Published online: ((will be filled in by the editorial staff))

References

[1] a) Y. Lu, W.-J. Yin, K.-L. Peng, K. Wang, Q. Hu, A. Selloni, F.-R. Chen, L.-M. Liu, M.-L. Sui, *Nat. Commun.* **2018**, *9*, 2752; b) H. You, Y. Jia, Z. Wu, F. Wang, H. Huang, Y. Wang, *Nat. Commun.* **2018**, *9*, 2889; c) L. Wang, Y. Wan, Y. Ding, S. Wu, Y. Zhang, X. Zhang, G. Zhang, Y. Xiong, X. Wu, J. Yang, H. Xu, *Adv. Mater.* **2017**, *29*; d) L. Wang, Y. Zhang, L. Chen, H. Xu, Y. Xiong, *Adv. Mater.* **2018**, *30*; e) Q. Y. Zeng, J. Bai, J. H. Li, B. X. Zhou, Y. G. Sun, *Nano Energy* **2017**, *41*, 225-232.

[2] L. Wang, X. Zheng, L. Chen, Y. Xiong, H. Xu, *Angew. Chem. Int. Edit.* **2018**, *57*, 3454-3458.

[3] a) M. Y. Wang, L. Sun, Z. Q. Lin, J. H. Cai, K. P. Xie, C. J. Lin, *Energy Environ. Sci.* **2013**, *6*, 1211-1220; b) H. Huang, K. Xiao, Y. He, T. Zhang, F. Dong, X. Du, Y. Zhang, *Appl. Catal. B-Environ.* **2016**, *199*, 75-86.

[4] M. Y. Wang, L. J. Cai, Y. Wang, F. C. Zhou, K. Xu, X. M. Tao, Y. Chai, *J. Am. Chem. Soc.* **2017**, *139*, 4144-4151.

[5] a) H. Li, Y. Sang, S. Chang, X. Huang, Y. Zhang, R. Yang, H. Jiang, H. Liu, Z. L. Wang, *Nano Lett.* **2015**, *15*, 2372-2379; b) Z. Wen, C. Li, D. Wu, A. D. Li, N. B. Ming, *Nat. Mater.* **2013**, *12*, 617-621.

[6] Z. L. Wang, *Nano Today* **2010**, *5*, 540-552.

[7] a) Y. F. Cui, J. Briscoe, S. Dunn, *Chem. Mater.* **2013**, *25*, 4215-4223; b) M. Wang, B. Wang, F. Huang, Z. Lin, *Angew. Chem. Int. Ed.* **2019**, *10.1002/anie.201811709*.

[8] H. W. Huang, S. C. Tu, C. Zeng, T. R. Zhang, A. H. Reshak, Y. H. Zhang, *Angew. Chem. Int. Edit.* **2017**, *56*, 11860-11864.

[9] a) X. Meng, X. Cui, M. Rager, S. Zhang, Z. Wang, J. Yu, Y. W. Harn, Z. Kang, B. K. Wagner, Y. Liu, C. Yu, J. Qiu, Z. Lin, *Nano Energy* **2018**, *52*, 123-133; b) M. He, B. Li, X. Cui, B. Jiang, Y. He, Y. Chen, D. O'Neil, P. Szymanski, M. A. El-Sayed, J. Huang, Z. Lin, *Nat. Commun.* **2017**, *8*; c) M. He, X. Pang, X. Liu, B. Jiang, Y. He, H. Snaith, Z. Lin, *Angew. Chem. Int. Edit.* **2016**, *55*, 4280-4284; d) H. Hu, L. Wu, Y. Tan, Q. Zhong, M. Chen, Y. Qiu, D. Yang, B. Sun, Q. Zhang, Y. Yin, *J. Am. Chem. Soc.* **2018**, *140*, 406-412; e) D. Chen, M. Qiao, Y.-R. Lu, L. Hao, D. Liu, C.-L. Dong, Y. Li, S. Wang, *Angew. Chem. Int. Ed.* **2018**, *57*, 8691-8696.

[10] a) N. H. Tiep, Z. Ku, H. J. Fan, *Adv. Energy Mater.* **2016**, *6*, 1501420; b) M. Z. Liu, M. B. Johnston, H. J. Snaith, *Nature* **2013**, *501*, 395-398.

[11] F. Zhou, Z. Ren, Y. Zhao, X. Shen, A. Wang, Y. Y. Li, C. Surya, Y. Chai, *ACS Nano* **2016**, *10*, 5900-5908.

[12] L. T. Dou, Y. Yang, J. B. You, Z. R. Hong, W. H. Chang, G. Li, Y. Yang, *Nat. Commun.* **2014**, *5*, 5404.

[13] H. M. Zhu, Y. P. Fu, F. Meng, X. X. Wu, Z. Z. Gong, Q. Ding, M. V. Gustafsson, M. T. Trinh,

S. Jin, X. Y. Zhu, *Nat. Mater.* **2015**, *14*, 636-642.

[14] M. Coll, A. Gomez, E. Mas-Marza, O. Almora, G. Garcia-Belmonte, M. Campoy-Quiles, J. Bisquert, *J. Phys. Chem. Lett.* **2015**, *6*, 1408-1413.

[15] S. Park, W. J. Chang, C. W. Lee, S. Park, H.-Y. Ahn, K. T. Nam, *Nature Energy* **2016**, *2*, 16185.

[16] E. B. Flint, K. S. Suslick, *Science* **1991**, *253*, 1397-1399.

[17] S. Liu, F. Zheng, I. Grinberg, A. M. Rappe, *J. Phys. Chem. Lett.* **2016**, *7*, 1460-1465.

[18] S. J. Jiang, Y. A. Fang, R. P. Li, H. Xiao, J. Crowley, C. Y. Wang, T. J. White, W. A. Goddard, Z. W. Wang, T. Baikie, J. Y. Fang, *Angew. Chem. Int. Edit.* **2016**, *55*, 6540-6544.

[19] B. C. Mohanty, Y. H. Jo, D. H. Yeon, I. J. Choi, Y. S. Cho, *Appl. Phys. Lett.* **2009**, *95*, 062103.

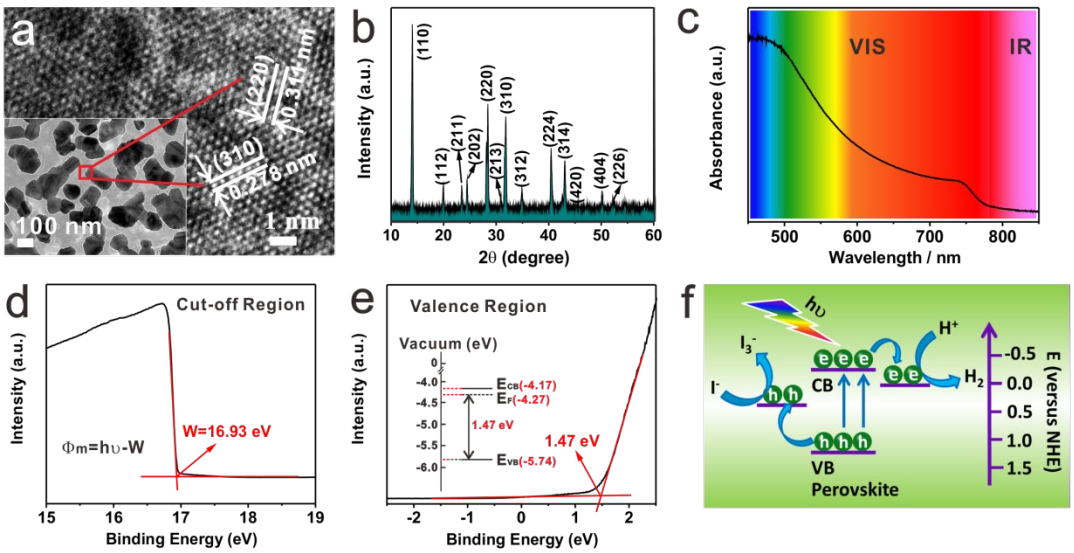

Figure 1. (a) High resolution TEM image of a selected area of $MAPbI_3$ marked in the low magnification image in the inset. (b) XRD pattern of $MAPbI_3$. (c) UV-vis absorption spectrum of $MAPbI_3$. (d-e) UPS spectra of $MAPbI_3$ at (d) cut-off region and (e) valence band region. ($h\upsilon$=21.2 eV). (f) The band structure of $MAPbI_3$ for hydrogen generation.

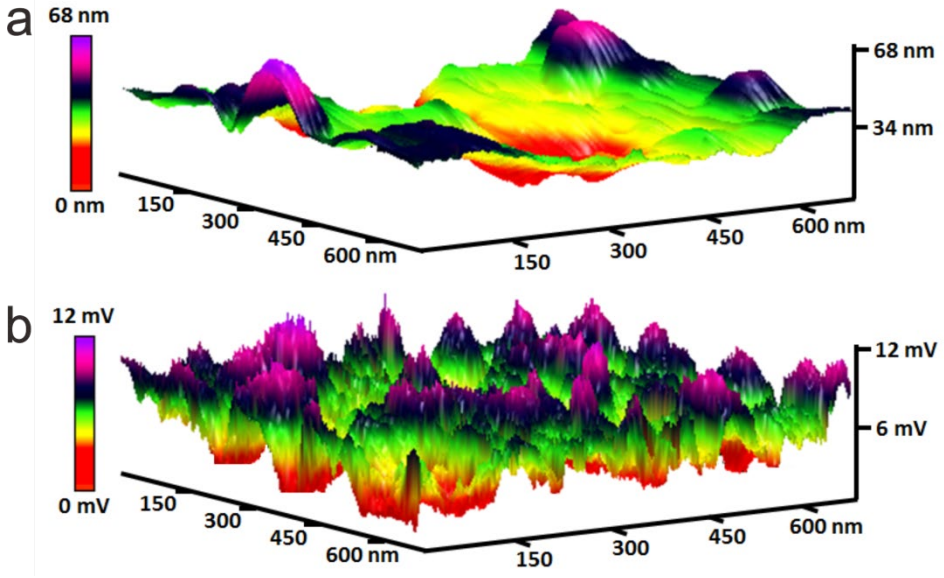

Figure 2. (a) Surface topography and (b) PFM amplitude of $MAPbI_3$ thin film.

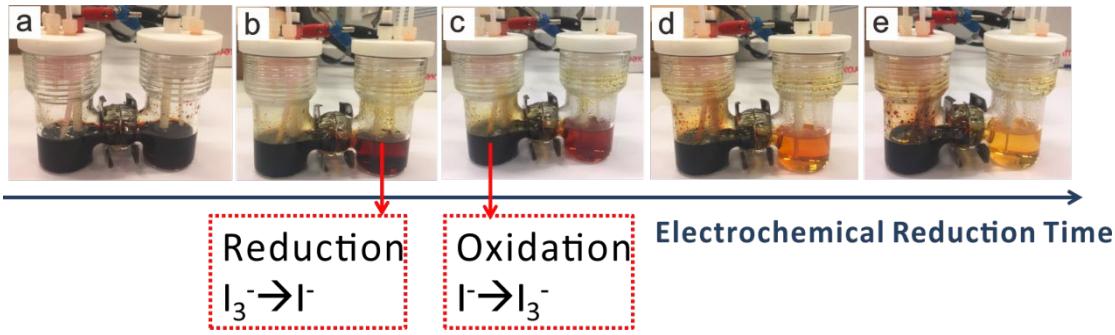

Figure 3. Digital images of HI solution under electrochemical treatment for (a) 0 h, (b) 0.5 h, (c) 1 h, (d) 1.5 h, and (e) 2 h, respectively. A proton exchange membrance (Nafion N117) is placed between the left and right compartments of the H cell. The I_3^- ions in the right compartment are continuously reduced to I^- ions as time progresses, the color of the HI solution is thus changed from dark purple to light yellow.

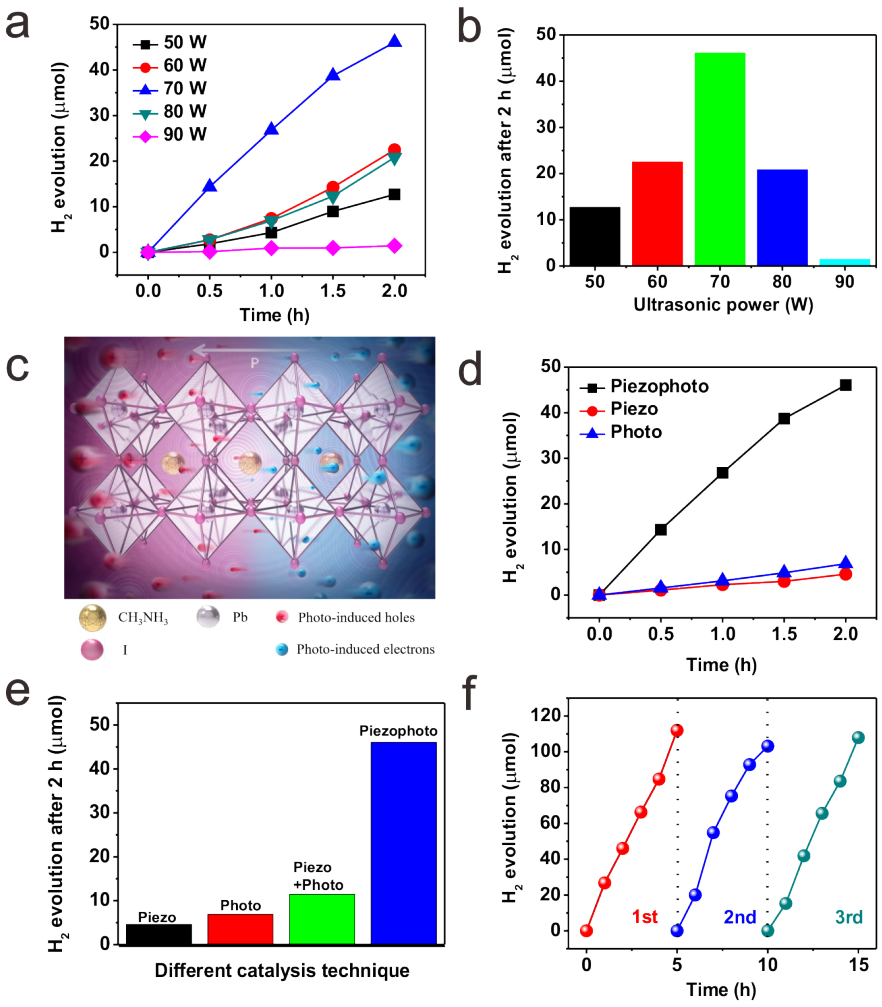

Figure 4. (a) Piezophoto-catalytic hydrogen evolution as a function of catalytic reaction time, and (b) the corresponding amount of hydrogen generated from $MAPbI_3$ after 2 h at ultrasonic power of 50 W, 60 W, 70 W, 80 W, and 90 W in the $MAPbI_3$-saturated HI solution. (c) Schematic illustration of the piezocatalytic mechanism of $MAPbI_3$. (d) Time-dependent piezophoto-catalytic, photocatalytic, piezocatalytic hydrogen evolution and (e) the corresponding amount of hydrogen generated from $MAPbI_3$ after 2 h in $MAPbI_3$-saturated HI solution, where the simple sum of photocatalytic and piezocatalytic hydrogen evolution is depicted by green bar. (f) Cycling performance of hydrogen generation for $MAPbI_3$ by piezophoto-catalysis at the ultrasonic power of 70 W.

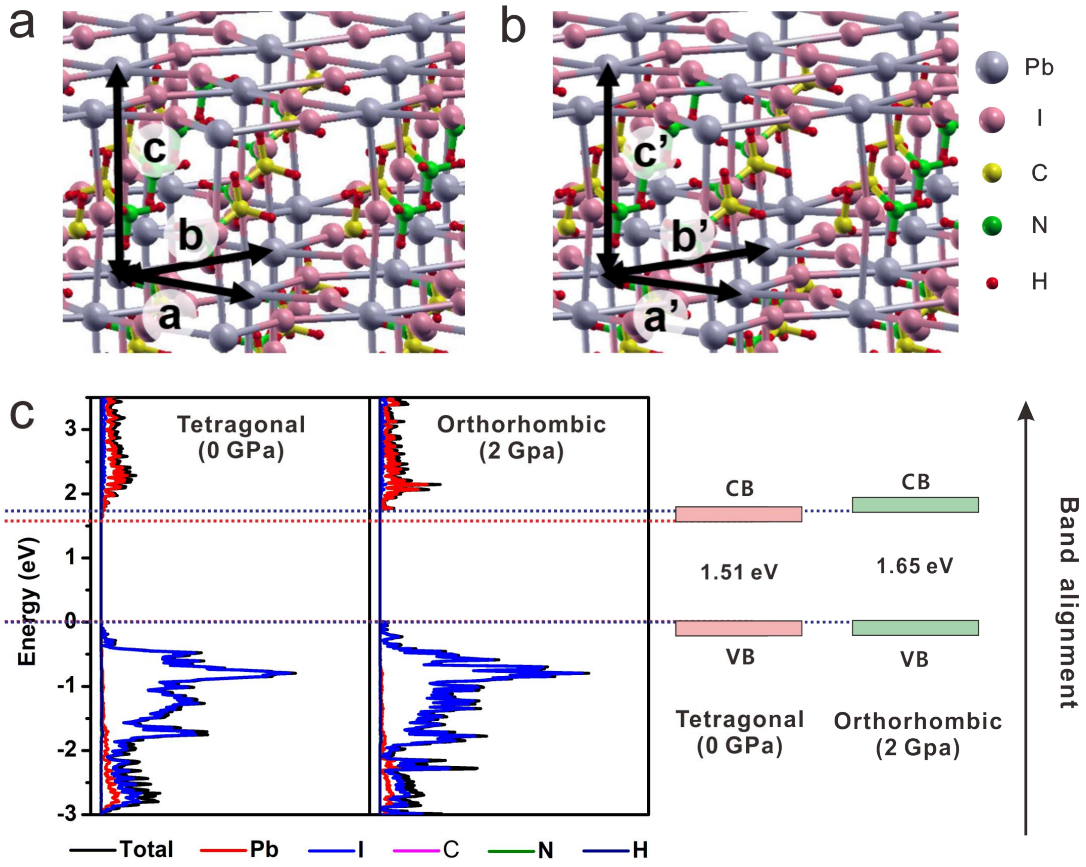

Figure 5. Atomic structures of $MAPbI_3$ under different mechanical pressures of (a) 0 GPa and (b) 2 GPa. (c) Calculated DOS (left panels) and band alignment (right panel) of $MAPbI_3$ under different mechanical pressure.

TOC

$CH_3NH_3PbI_3$ exhibits superior piezophoto-catalytic hydrogen generation rate upon concurrent light and mechanical stimulations, much higher than that of piezocatalytic and photocatalytic hydrogen evolution rate as well as their sum. Combining piezo-catalysis and photo-catalysis of semiconductor photocatalysts to attain a collective piezophoto-catalysis may represent an appealing strategy for efficient solar energy conversion, including water splitting, organic fuel production, *etc*.

Keywords: Piezophoto-catalysis, $CH_3NH_3PbI_3$ perovskite, piezoelectrics, hydrogen generation

*Mengye Wang,[1,2] Yunpeng Zuo,[2] Jingli Wang,[2] Yi Wang,[2] Xinpeng Shen,[2] Bocheng Qiu,[2] Lejuan Cai,[2] Feichi Zhou,[2] Shu Ping Lau[2] and Yang Chai[2,]**

Remarkably Enhanced Hydrogen Generation of Organolead Halide Perovskites via Piezocatalysis and Photocatalysis